Applied Thermal Engineering 123 (2017) 1278–1290

Contents lists available at ScienceDirect

Applied Thermal Engineering

journal homepage: www.elsevier.com/locate/apthermeng

A two-dimensional model of regenerator with mixed matrices and experimental verifications for improving the single-stage Stirling-type pulse tube cryocooler

Dingli Bao [a,b], Jun Tan [a], Lei Zhang [c], Zhiqian Gao [a,b], Yibo Zhao [a,b], Haizheng Dang [a,*]

[a] National Laboratory for Infrared Physics, Shanghai Institute of Technical Physics, Chinese Academy of Sciences, 500 Yutian Road, Shanghai 200083, China
[b] University of Chinese Academy of Sciences, No.19A Yuquan Road, Beijing 100049, China
[c] AECC Commercial Aircraft Engine Co., LTD., 3998 Lianhua South Road, Shanghai 200241, China

HIGHLIGHTS

- A 2D regenerator model for optimizing the mixed matrices is introduced.
- Pressure and heat transfer characteristics with different matrices are discussed.
- Simulation results are verified by the experiments based on a coaxial SPTC.
- Only conventional SS matrices are used excluding both double-inlet and multi-bypass.
- A no-load temperature of 26.7 K and 0.45 W at 30 K are achieved with 220 W of input.

ARTICLE INFO

Article history:
Received 23 January 2017
Revised 11 May 2017
Accepted 27 May 2017
Available online 31 May 2017

Keywords:
Two-dimensional model
Regenerator with mixed matrices
Filling proportion
Stainless steel screen
Single-stage Stirling-type pulse tube cryocooler
Experimental verification

ABSTRACT

A two-dimensional regenerator model based on Brinkman-Forchheimer equations is established to obtain a model with fast speed and acceptable accuracy. To improve the performance of the Stirling-type pulse tube cryocooler (SPTC), the different filling proportions of mixed matrices made of stainless steel (SS) screens are simulated and compared, and then the optimal proportion is suggested. The analyses are mainly focused on the cooling performance and the losses caused by the different entropy generations. The experiments are then conducted to verify the theoretical investigations based on a single-stage coaxial SPTC, in which the cooling characteristics with various frequencies and temperatures are tested and then compared with the analyses. The results show a good agreement between the simulations and the experiments. The cooling performance can be enhanced based on the optimized mixed matrix, in which for a reject temperature of 300 K and an input electric power of 220 W, the SPTC has experimentally achieved the cooling capacity of 0.45 W at 30 K and a no-load temperature of 26.7 K. The performance is impressive considering that only the conventional SS matrices are employed and neither double-inlet nor multi-bypass phase-shifting approach is used.

1. Introduction

The cryocoolers can be generally classified as either recuperative or regenerative, in which the latter uses at least one regenerator and operates with the oscillating flow and pressure [1]. For the typical regenerative cryocooler such as the GM cryocooler, the Stirling cryocooler and the pulse tube cryocooler (PTC). The regenerator is one of the key components because the irreversible loss caused in it usually accounts for an overwhelming proportion of the overall losses, and thus the cooling efficiency of a regenerative cryocooler depends on the performance of the regenerator to a great degree [2].

Generally speaking, the performance of a regenerator is mainly determined by the heat capacity of the matrix, the heat transfer between matrix and fluid, the conductive heat loss from hot to cold ends, and the pressure drop of the flow through the porous media. Some of them are conflicting requirements. For example, the good heat transfer between matrix and fluid will make a very positive contribution to the enhancement of the regenerator performance, but to improve the heat transfer needs to decrease the porosity of the matrix and then increase the pressure drop, thereby resulting in the correspondingly greater pressure drop loss.

* Corresponding author.
E-mail address: haizheng.dang@mail.sitp.ac.cn (H. Dang).

http://dx.doi.org/10.1016/j.applthermaleng.2017.05.152
1359-4311/

Nomenclature

A	cross-section area, m^2
c_p	specific heat capacity of the gas
c_s	specific heat capacity of the matrix
d_h	hydraulic diameter, m
E	time-averaged energy flux, W
f	operating frequency, Hz
F	inertia coefficient
H	time-averaged enthalpy
h	convective heat transfer coefficient
i	imaginary unit
Im[]	imaginary part
k	overall thermal conductivity
K	permeability
L	tube length, m
$\dot{m}$	mass flux
m	pressure derivative by x
p	pressure, Pa
p_0	charge pressure, Pa
Pr	Prandtl number
R	tube radius, m
R_g	gas constant, 2.0785 J/g·K, for helium
Re[]	real part
r_e	equivalent radius, m
T	temperature, K
t	time, s
u	axial velocity, m/s
W	time-averaged *PV* work, W
Z	compression factor

Greeks

α	specific surface area
β	coefficient of expansion
δ	penetration depth
μ	viscosity
ρ	density
σ	heat capacity ratio
Φ	porosity
φ	phase angle
ω	angular velocity

Subscripts

1	first-order
2	second-order
c	cold end
e	equivalent
g	gas
h	hot end
i	inlet
k	thermal
n	node number
m	mean value
o	outlet
s	solid
v	viscous

Several theoretical analyses or simulations about the regenerators were reported. For example, Swift [3] described a simple harmonic analysis of the performance of regenerators based on one-dimensional differential equations of heat and mass flow. Ju et al. [4] carried out the numerical simulation and experimental verification of the oscillating flow in the regenerator, and Hao and Ju [5] performed the experimental study on the low temperature regenerator packed with rectification meshes. He et al. [6] carried out the two-dimensional numerical simulation and performance analysis of tapered pulse tube refrigerator, and proposed a modeling approach for the performance of pulse tube refrigerator by combining one-dimensional and two-dimensional models together [7]. Xu and Morie [8] developed a numerical simulation program to predict the theoretical cooling capacity and losses in regenerators. Dang et al. [9] developed an improved ECA model to investigate the cold finger characteristics and their influences on the linear compressor, and a two-dimensional axis-symmetric CFD model of the single-stage coaxial Stirling-type PTC is also established [10], in which the losses of the regenerator with fixed mixed matrices was discussed and then verified by the experiment.

In the one-dimensional models, the radial direction dependence of the temperature vibration is neglected, and thus the simulation results are greatly affected. Therefore, many two-dimensional models have been developed to consider both the viscous and the heat penetration depth effects and to improve the accuracy of the model. The two-dimensional CFD model based on the Fluent® software [11] is a popular approach to describe the instantaneous internal fluid mechanism in a more detailed way [10]. However, normally it is time-consuming and takes much computation resources to achieve stability. In this paper, a two-dimensional regenerator model with fast speed and acceptable accuracy will be built for the SPTC. Speaking broadly, the developed model can also be regarded as a type of CFD approach, but it is based on the Harmonic Approximation Method with acceptable small reductions in accuracy, which omits the high-order variables and keeps the first-order variables. The four-order Runge–Kutta method will be used to discrete the analytical solutions and solve the continuous variables along the length. In the later experiments, it can be seen that the results of the developed model in this paper is close to the one of the conventional CFD model based on Fluent®.

Based on the developed model, the regenerator of the SPTC with neither double-inlet nor multi-bypass phase-shifting will be optimized. To improve the performance of the SPTC, the different filling proportions of mixed matrices made of stainless steel screens are studied and compared, and then the optimal proportion is suggested. As shown later, the results of the simulations are verified by the experiments. And the SPTC performance is improved impressively by the suggested filling proportion. The developed model with fast speed and acceptable accuracy in this research provides the theoretical guides of optimizing the filling proportion of the regenerator and analyzing the loss mechanism.

2. Model

2.1. Geometry

Fig. 1 shows a two-dimensional axis-symmetric regenerator model. The regenerator is regarded as an isotropic porous media, and its length, radius and porosity are L, R and Φ, respectively. The hot end at the left is the inlet while the cold end at the right is the outlet. T_h, u_1, p_1 at the inlet and T_c at the outlet are the boundary parameters. The working parameters include the frequency f, the charge pressure p_0, the permeability coefficient K and the inertia coefficient F. The orifice in the regenerator matrix can be regarded as a circle with an equivalent radius of r_e, in which both viscous and heat penetration depths are the radial parameters which change significantly with the temperature.

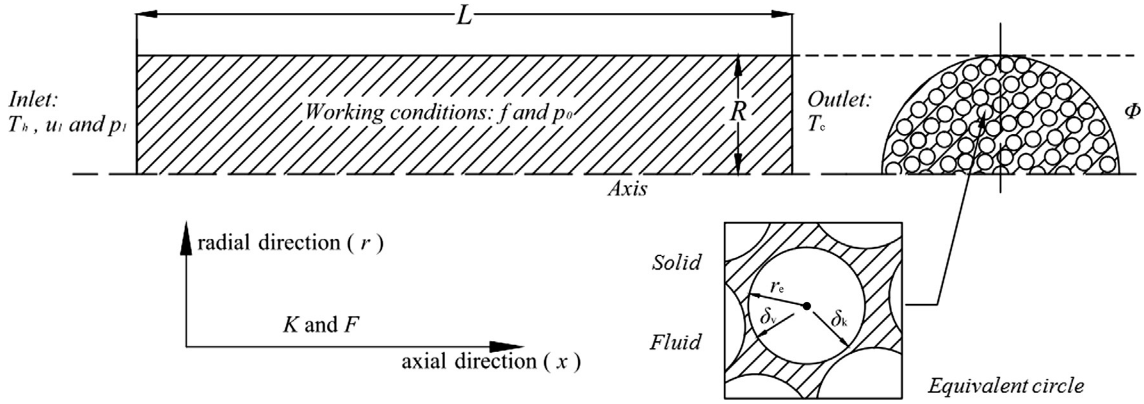

Fig. 1. Schematic diagram of a regenerator model.

2.2. Governing equation

The two dimensional Brinkman–Forchheimer equations for the isotropic porous media model can be written as follows [12]:

$$\phi\frac{\partial\rho}{\partial t}+\nabla\cdot(\rho\mathbf{v})=0 \tag{1}$$

$$\rho\left(\frac{\partial\mathbf{v}}{\partial t}+\nabla(\phi^{-1}\mathbf{v}\cdot\mathbf{v})\right)=-\phi\nabla p+\mu\nabla^2\mathbf{v}-\phi\frac{\mu}{K}\mathbf{v}-\frac{F\rho\phi}{\sqrt{K}}|\mathbf{v}|\mathbf{v} \tag{2}$$

$$\phi\rho c_p\frac{\partial T_g}{\partial t}+\rho c_p\mathbf{v}\cdot\nabla T_g=\phi\nabla\cdot(k_g\nabla T_g)+\beta T_g\phi\left[\frac{\partial p}{\partial t}-\mathbf{v}\cdot\left(\frac{\mu}{K}\mathbf{v}+\frac{F\rho}{\sqrt{K}}|\mathbf{v}|\mathbf{v}\right)\right] \tag{3}$$

$$(1-\phi)\rho_s c_s\frac{\partial T_s}{\partial t}=(1-\phi)\nabla\cdot(k_s\nabla T_s) \tag{4}$$

where Eqs. (1) and (2) are the continuity and momentum equations for the gas, respectively. Eqs. (3) and (4) are the energy equation for the gas and matrix, respectively.

The main assumptions used in the analysis are as follows:

(1) The acoustic approximation is valid (low Mach number regime).
(2) The pressure variation in radial direction can be neglected.
(3) The variables are expressed in complex notation, such as:

$$\rho=\rho_m(x)+\rho_1(x,r)e^{i\omega t},\quad \mu=\mu_m(x)+\mu_1(x,r)e^{i\omega t},\quad p=p_m+p_1(x)e^{i\omega t},$$
$$T=T_m(x)+T_1(x,r)e^{i\omega t},\quad u=u_1(x,r)e^{i\omega t}\ \text{and}\ v=v_1(x,r)e^{i\omega t}.$$

(4) The temperature of the matrix is the same as that of the gas at the interface.

Under the above assumptions, the conservation equations of the mass and the momentum, the equation includes both the gas and solid energy equations, and the real gas equation can be written as follows:

$$\frac{\partial\rho}{\partial t}+\frac{\partial(\rho u)}{\partial x}+\frac{1}{r}\frac{\partial(r\rho v)}{\partial r}=0 \tag{5}$$

$$\rho\left(\frac{\partial u}{\partial t}+\phi^{-1}u\frac{\partial u}{\partial x}+\phi^{-1}v\frac{\partial u}{\partial r}\right)+\frac{F\rho\phi}{\sqrt{K}}u^2=-\phi\frac{\partial p}{\partial x}-\phi\frac{\mu}{K}u+\frac{1}{r}\frac{\partial}{\partial r}\left(r\mu\frac{\partial u}{\partial r}\right) \tag{6}$$

$$\rho c_p\left(\sigma\frac{\partial T}{\partial t}+u\frac{\partial T}{\partial x}+v\frac{\partial T}{\partial r}\right)=\frac{1}{r}\frac{\partial}{\partial r}\left(rk\frac{\partial T}{\partial r}\right)+\beta T_g\phi\left(\frac{\partial p}{\partial t}-\frac{\mu}{K}u^2-\frac{F\rho}{\sqrt{K}}u^3\right) \tag{7}$$

$$p=Z\rho R_g T \tag{8}$$

where the variables in the angle brackets mean the cross-section averaged ones, and the porous medium heat capacity ratio σ and the overall thermal conductivity k can be defined as follows:

$$\sigma=\phi+(1-\phi)(\rho_s c_s)/(\rho_g c_p) \tag{9}$$

$$k=(1-\phi)\lambda k_s+\phi k_g \tag{10}$$

where λ is the conduction degradation factor of the matrix [13].

According to the acoustic approximation, the first-order equations are expressed as:

$$i\omega\langle\rho_1\rangle+\frac{\partial\langle\rho_m u_1\rangle}{\partial x}=0 \tag{11}$$

$$i\omega\rho_m u_1+\frac{F\phi\rho_m}{\sqrt{K}}u_0^2=-\phi\frac{\partial p_1}{\partial x}-\phi\frac{\mu}{K}u_1+\frac{1}{r}\frac{\partial}{\partial r}\left(r\mu\frac{\partial u_1}{\partial r}\right) \tag{12}$$

$$i\omega\rho_m c_p\sigma T_1+\rho_m c_p u_1\frac{\partial T_m}{\partial x}=\frac{1}{r}\frac{\partial}{\partial r}\left(rk\frac{\partial T_1}{\partial r}\right)+i\phi\omega\beta T_m p_1 \tag{13}$$

$$\langle\rho_1\rangle=\frac{\langle p_1\rangle}{ZR_gT_m}-\rho_m\frac{\langle T_1\rangle}{T_m} \tag{14}$$

And the term u^2 in Eq. (6) is expressed as a Taylor series and approximated to the following form [14]:

$$u^2\approx u_0^2+2(u-u_0)u_0+(u-u_0)^2 \tag{15}$$

Truncating the above series after the first term. The determination process of u_0 is showed in the flow chart in Section 3.2.

After the following boundary conditions at $r=0$, $\partial u_1(T_1)/\partial r=0$ and at $r=R$, $u_1(T_1)=0$ are applied, for circular pores of radius the solutions to Eqs. (12) and (13) becomes:

$$u_1=\frac{i}{\alpha^2}\left(\frac{\phi}{\omega\rho_m}\frac{\partial p_1}{\partial x}+\frac{F\phi}{\omega\sqrt{K}}u_0^2\right)(1-h_v) \tag{16}$$

$$T_1=\frac{\phi\beta T_m p_1}{\rho_m c_p\sigma}(1-h_k)-\frac{1}{\omega\sigma\alpha^2}\times\frac{\partial T_m}{\partial x}\left(\frac{\phi}{\omega\rho_m}\frac{\partial p_1}{\partial x}+\frac{F\phi}{\omega\sqrt{K}}u_0^2\right)\left(1-\frac{Pr\sigma}{Pr\sigma-\alpha^2}h_v+\frac{\alpha^2}{Pr\sigma-\alpha^2}h_k\right) \tag{17}$$

By using the integration, $\langle F\rangle = 1/A\int_R^0 F(r)dA = 2/R^2\int_R^0 F(r)rdr$, the cross-section average velocity and temperature amplitude are gotten as follows:

$$\langle u_1\rangle = \frac{i}{\alpha^2}\left(\frac{\phi}{\omega\rho_m}\frac{\partial p_1}{\partial x} + \frac{F\phi}{\omega\sqrt{K}}u_0^2\right)(1-f_v) \tag{18}$$

$$\langle T_1\rangle = \frac{\phi\beta T_m p_1}{\rho_m c_p\sigma}(1-f_k) - \frac{1}{\omega\sigma\alpha^2} \times \frac{\partial T_m}{\partial x}\left(\frac{\phi}{\omega\rho_m}\frac{\partial p_1}{\partial x} + \frac{F\phi}{\omega\sqrt{K}}u_0^2\right)\left(1 - \frac{Pr\sigma}{Pr\sigma-\alpha^2}f_v + \frac{\alpha^2}{Pr\sigma-\alpha^2}f_k\right) \tag{19}$$

where

$$\alpha = \sqrt{1+\phi\delta_v^2/(2iK)} \tag{20}$$

The complex function h and its spatial-average function f can be expressed as follows [15]:

For viscous complex and spatial-average functions:

$$h_v = \frac{J_0[(i-1)\alpha S_w Y]}{J_0[(i-1)\alpha S_w]} \tag{21}$$

$$f_v = \frac{2J_1[(i-1)\alpha S_w]}{J_0[(i-1)\alpha S_w](i-1)\alpha S_w} \tag{22}$$

For thermal complex and spatial-average functions:

$$h_k = \frac{J_0[(i-1)\sqrt{\sigma Pr}S_w Y]}{J_0[(i-1)\sqrt{\sigma Pr}S_w]} \tag{23}$$

$$f_k = \frac{2J_1[(i-1)\sqrt{\sigma Pr}S_w]}{J_0[(i-1)\sqrt{\sigma Pr}S_w](i-1)\sqrt{\sigma Pr}S_w} \tag{24}$$

where $J_0[\ ]$ and $J_1[\ ]$ are zero-order and first-order Bessel function, respectively.

2.3. Derivations of K and F

The axial permeability K and the inertia coefficient F could be gotten based on the experimental data. And the oscillating flow friction factor for woven screen is given as [16]:

$$f_{osc} = 39.52/Re + 0.01 \tag{25}$$

where Re is Reynolds, and the functions of K and F are:

$$K = d_h^2/79.4 \tag{26}$$

$$F = 0.02\sqrt{K}/(\phi d_h) \tag{27}$$

2.4. Properties of fluid and matrix

The property of the helium gas varies significantly with the changing temperature. The property parameters dependent on the temperature including the heat capacity c_p and the thermal conductivity k_g of the gas, the heat capacity c_s and the thermal conductivity k_s of the matrix are gotten from Ref. [17].

And the viscosity μ of the gas is expressed as [18]:

$$\mu_m(T) = \mu_0(T/T_0)^b \tag{28}$$

where $b = (T_m/\mu_m)(d\mu_m/dT_m) \approx 0.68$.

The viscous and heat penetration depths dependent on the temperature are defined as:

$$\delta_v(T) = \sqrt{2\mu_m(T)/\omega\rho_m(T)} \tag{29}$$

$$\delta_k(T) = \delta_v(T)/\sqrt{Pr} \approx \delta_v(T)/\sqrt{0.69} \tag{30}$$

The real gas effects become evident below about 40 K. The compression factor is used to correct the mean density as follows:

$$\rho_m = p_0/(ZR_gT_m) \tag{31}$$

2.5. Regenerator performance

The time-averaged and cross-section-averaged energy flux along the axial-direction is independent of x because of the energy conservation.

$$E_2 = H_2 + Q_k = \text{const} \tag{32}$$

Then the time-averaged energy flux is:

$$\begin{aligned} E_2 &= \left[\rho_m c_p\int Re(\tilde{u}_1T_1)dA_e + (1-T_m\beta)\int Re(\tilde{p}_1u_1)dA_e\right]\times(A/2A_e) - AkdT_m/dx \\ &= \left[\pi\rho_m c_p\int_0^{r_e} Re(\tilde{u}_1T_1)rdr + \pi(1-T_m\beta)\int_0^{r_e} Re(\tilde{p}_1u_1)rdr\right] \times \phi R^2/r_e^2 - \pi R^2kdT_m/dx \end{aligned} \tag{33}$$

For the ideal gas, $(1 - T_m\beta) = 0$.

And the time-averaged PV work is:

$$\begin{aligned} W_2 &= \int Re(\tilde{p}_1u_1)dA_e \times (A/2A_e) \\ &= \pi\int_0^{r_e} Re(\tilde{p}_1u_1)rdr \times \phi R^2/r_e^2 \end{aligned} \tag{34}$$

The cooling capacity at the cold end and the COP of the regenerator are expressed as:

$$Q_c \approx W_2(cold) - H_2(cold) - Q_{cond}(cold) = W_2(cold) - E_2 \tag{35}$$

$$COP = Q_c/W_2(hot) \tag{36}$$

3. Numerical method

3.1. Solutions of the governing equations

Let $dp_1/dx = m$, then $d^2p_1/dx^2 = dm/dx$. And thus the mean temperature T_m derivative equation and first-order pressure p_1 second derivative equation are expressed as follows:

$$\begin{cases} g_1(T_m) = \frac{dT_m}{dx} = (E_2 - X_1 + X_3)/(X_2 - \pi R^2k) \\ g_2(m) = \frac{dm}{dx} = Y_1\cdot p_1 - Y_2\cdot p_1/T_m + Y_3\cdot g_1(T_m)\cdot m/T_m + Y_4\cdot g_1(T_m)/T_m \\ g_3(p_1) = \frac{dp_1}{dx} = m \end{cases} \tag{37}$$

The three variables in the above three equations can be solved. The derivation and the coefficients in the equations are given in Appendix A.

The initial parameters at the inlet are given, which include T_h, $|u_1|$, $|p_1|$ and the positive phase angle φ between the amplitude pressure and the velocity. Let $u_1^1 = |u_1|$, m^1 can be obtained from Eq. (18) and the expressions of other initial variable are gotten as follows:

$$T_m^1 = T_h \tag{38}$$

$$p_1^1 = |p_1|\cos(\varphi) \pm i\times|p_1|\sin(\varphi) \tag{39}$$

$$T_m^{L1} = T_c \tag{40}$$

The plus and minus signs in Eq. (39) depend on the experimental data in which the velocity leads or lags the pressure. The velocity usually leads the pressure at inlet and the equation takes the minus sign. In this paper, the dynamic pressure and the fluctuating velocity, both of which are derived from the two-dimensional porous media equations, will combine with the energy conservation equation to simulate the parameters along the regenerator length and the cooling capacity of the SPTC's regenerator.

3.2. Numerical method and flow chart

The conventional finite volume method is hard to solve equation set (37). The main reason is that the equation set (37) includes both the imaginary part of p_1 and the conjugate form of p_1, which make the equations hard to discrete. The Runge-Kutta method is employed here to make the numerical calculation [19,20]. The flow chart is shown in Fig. 2, which consists of the following steps:

(1) The initial boundary variables are set by Eqs. (38), (39) and (40). The working conditions and dimensional parameters are given. In addition, u_0 is estimated by Eq. (18) at first cycle.
(2) The initial energy flux E_2 is estimated by Eq. (33) and the initial variables at the inlet together. And the initial adjusted value E_c is set as one percent of E_2.
(3) The calculation starts from node 1 to node L_1, the range of the nodes are controlled from 60 to 100. Too few nodes will cause errors, while too many ones will take more calculation time.
(4) The temperature T_m^{L1} at the outlet will be compared with the expected cold end temperature T_c. If the error $|T_m^{L1} - T_c|/T_c$ is kept below $\pm 0.02\%$, the program will move to the next step. Otherwise, the energy flux E_2 should be adjusted based on the adjusted value E_c and then repeat step (3) until $T_m^{L1} \cong T_c$ is satisfied.
(5) Let $u_0^n = u_1^n$ at each node and repeat step (1) until the error $|u_1^{L1} - u_0^{L1}|/u_0^{L1}$ at the node L_1 is kept below $\pm 0.5\%$ at the cold end. Then the program exports the outputs and finishes.

4. Theoretical optimization and experiments

4.1. Theoretical optimization

The performance of the conventional stainless steel (SS) screen matrix at lower temperatures such as 50 K becomes worse because its heat capacity decreases significantly with the decreasing temperature. In order to increase the regenerator's performance, the multi-layer method is often suggested [21,22]. There exits an optimal proportion for the mixed matrices to meet the conflicting requirements. The initial working conditions and boundary parameters of the model are similar to Ref. [9]. The frequency is 54 Hz, the pressure amplitude is 0.365 MPa, the velocity is 4.51 m/s and their phase angle is 0.078π. The dimensional parameters of the cold finger are shown in Table 1. The hydraulic diameters shown in Table 2 for 400-mesh, 500-mesh and 635-mesh SS screens are 55.24, 39.60 and 31.28 μm, respectively. In the model, the interface of different layers of the SS screens should meet the requirements as follows:

$$T_{m.l} = T_{m.r} \tag{41}$$

$$p_{1.l} = p_{1.r} \tag{42}$$

$$\dot{m}_l = \dot{m}_r \tag{43}$$

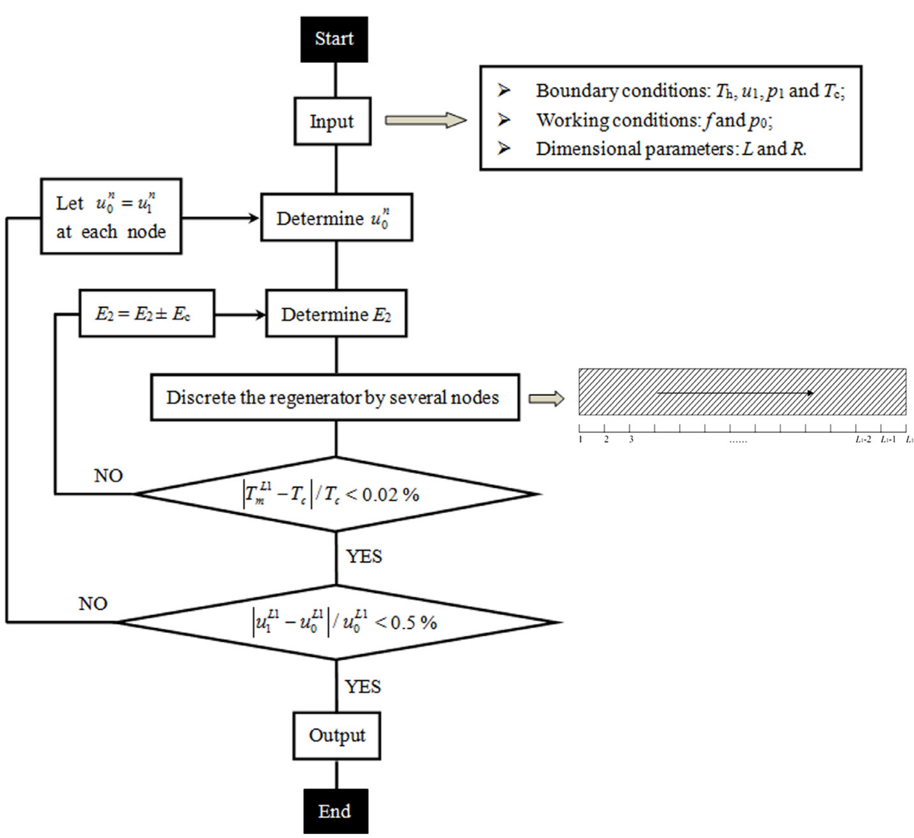

Fig. 2. Flow chart of the program.

Table 1
Parameters of the pulse tube cold finger.

Parameters	Values
Regenerator outer diameter	28.7 mm
Regenerator length	65 mm
Pulse tube diameter	13.0 mm
Pulse tube length	95 mm
Inertance tube I diameter	3.7 mm
Inertance tube I length	2250 mm
Inertance tube II diameter	7.6 mm
Inertance tube II length	4100 mm
Reservoir volume	400 cm^3

Table 2
Geometrical parameters of different SS screen meshes.

Mesh	Wire diameter (μm)	Porosity	d_h (μm)	r_e (μm)
400	25.4	0.685	55.24	27.62
500	25.0	0.613	39.60	19.80
635	20.0	0.607	31.28	15.64

where the subscript "l" means the left side of the interface while the subscript "r" means the right side of it.

Fig. 3(a) shows the variations of the cooling capacity with different filling proportions of 400-mesh and 500-mesh SS screens. The x-coordinate is the percentage of the segment with 400-mesh SS screen to the length. The filling combination is 400-mesh and 500-mesh SS screens. The 400-mesh SS screen is filled in the higher temperature part of the regenerator. The length of the regenerator is 65 mm and the cold end temperature is 60 K. The results indicate that there exits an optimal filling proportion and the cooling capacity is 3.82 W when the proportion is 40:25.

Fig. 3(b) shows the amounts of three entropy generations with different filling proportions of 400-mesh and 500-mesh SS screens. The vertical coordinate means the ratio of the segment of 400-mesh SS screen to the whole length (65 mm). In the regenerator, the entropy generations caused by the heat conduction for both matrix and gas, pressure drop and heat transfer are written as follows, respectively [23]:

$$S_c = \int A[\phi k_g + (1-\phi)k_s](dT_m/dx)^2/T_m^2 \cdot dx \tag{44}$$

$$S_p = \int -\dot{m}R(dp_1/dx)/p_0 \cdot dx \tag{45}$$

$$S_h = \int \frac{2\pi^2 c_s^2 \rho_s^2 A(1-\phi)^2 f^2}{\alpha h} \cdot \left(\frac{T_s}{T_m}\right)^2 dx \tag{46}$$

In Fig. 3(b), the conduction entropy generation increases slightly when the proportion of 500-mesh SS screen grows. According to Eq. (44), both the mean temperature and its gradient change slightly. The thermal conduction for the solid is larger than that for gas. When the segment of 400-mesh SS screen is replaced by that of 500-mesh SS screen, the porosity of this segment decreases, and thus the overall thermal conductivity increases. Therefore, the conduction entropy generation increases. Fig. 3(b) also indicates that the pressure drop entropy generation increases while the heat transfer entropy generation decreases when the proportion of 500-mesh SS screen grows. The reason is that the segment of 500-mesh SS screen has the smaller porosity compared to that of 400-mesh one, which causes the larger friction factor and also the larger entropy generation. However, the smaller hydraulic diameter can enhance the heat transfer efficiency and decrease the heat transfer entropy generation. Therefore, there exists an optimal ratio. For the cases in Fig. 3(b), the case (40/65) has the minimal total entropy generation and thus it has largest cooling capacity.

Fig. 4(a) shows the filling proportions of the mixed matrices for different cases and the respective cooling capacity. The cases from Case 1 to Case 4 which have the best cooling capacities among the cases in Fig. 3(a) are filled with 400-mesh and 500-mesh SS screens. The cases from Case 5 to Case 12 are filled with 400-mesh, 500-mesh and 635-mesh SS screens with various proportions. The cases from Case 5 to Case 11 are based on Case 2, Case 3 and Case 4, respectively, in which the segment of 500-mesh SS screen is replaced by 500-mesh and 635-mesh SS screens with various proportions to improve the cooling capacity. The filling proportion of Case 12 is 1:3:1 [10]. Case 13 and Case 14 are filled with constant matrix 400-mesh and 500-mesh SS screens, respectively. It is observed that the optimal performance (3.96 W) occurs in Case 8 with three-layer matrices which has a balance of the pressure loss and the heat transfer efficiency. The filling proportion of Case 8 is 9:1:3. Compared with Case 12 and Case 13, under the

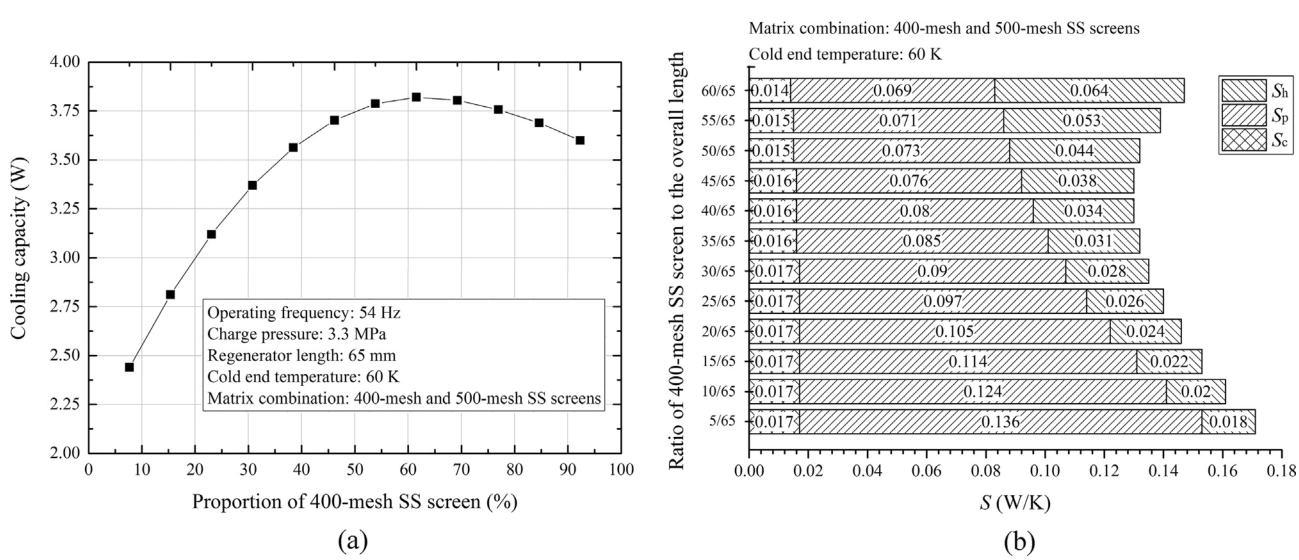

Fig. 3. (a) Variations of the cooling capacity with different filling proportions of 400-mesh and 500-mesh SS screens; (b) Amounts of three entropy generations with different filling proportions of 400-mesh and 500-mesh SS screens.

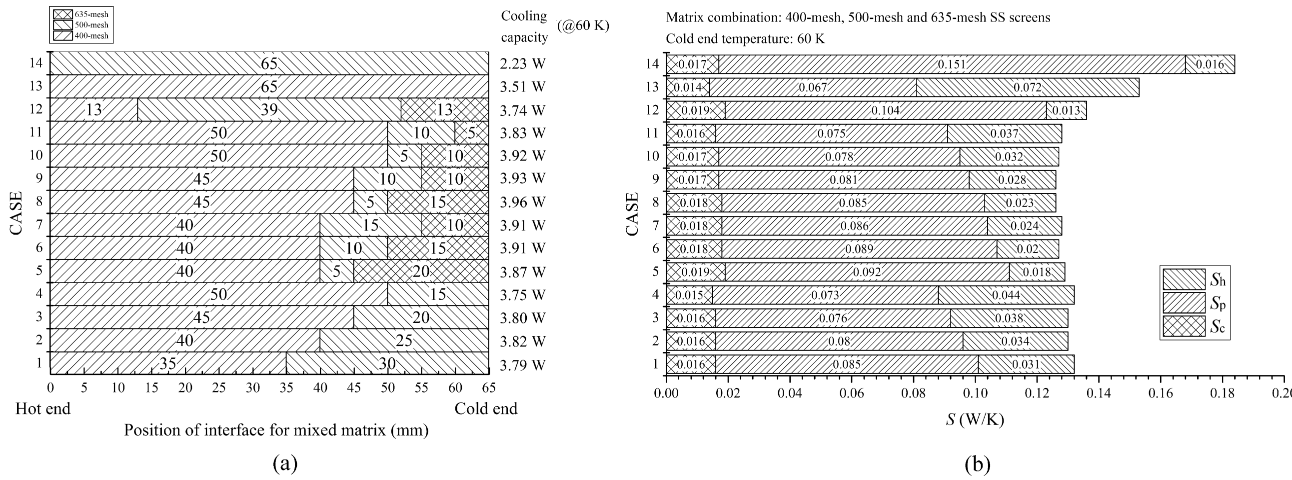

Fig. 4. (a) Filling proportions of the mixed matrices for different cases and the respective cooling capacity; (b) Amounts of three entropy generations for different cases in (a).

same boundary conditions, the cooling capacities of Case 8 increase by 5.89% and 12.82%, respectively.

Fig. 4(b) shows the amounts of three entropy generations for different cases in Fig. 4(a). It indicates that Case 14 with the constant 500-mesh SS screens has the largest total entropy generation and also the largest pressure drop loss. Case 13 with the constant 400-mesh SS screens has the second largest total entropy generation and also the largest heat transfer entropy generation. For the three-layer-matrices cases, Case 8 has the minimal total entropy generation among all the cases, and Case 12 has the third largest total entropy generation even if it has the smallest heat transfer entropy generation. The results indicate that there exits an optimal proportion for the mixed matrices.

Fig. 5 shows the variations of the pressure amplitude for Case 1, Case 2, Case 3, Case 8 and Case 9 along the length, respectively. The cold end temperature is set at 30 K for these cases. The turning points are the interfaces of the mixed matrices. The pressure drops are 0.096 MPa, 0.091 MPa, 0.086 MPa, 0.101 MPa and 0.095 MPa for Case 1, Case 2, Case 3, Case 8 and Case 9, respectively. For Case 1, Case 2 and Case 3, it indicates that the larger the rate of the 500-mesh SS screen, the larger pressure drop for two-layer matrices is. The Case 3, Case 8 and Case 9 have the same rate of the 400-mesh SS screen and the results indicate that if the regenerator has the larger rate of the 635-mesh SS screen, the pressure drop will become larger. It can be observed that the pressure gradient becomes largest in the part of the regenerator filled with 635-mesh because it has the smallest porosity and thus results in the largest resistance.

Fig. 6 shows the variations of the velocity amplitude of Case 1, Case 2, Case 3, Case 8 and Case 9 along the length, respectively. It can be found that there exits the turning points at the interface of the mixed matrices because the mass flow passes through the matrices with different porosities. When the porosity becomes smaller, the velocity will be larger and the velocity gradient will increase.

The equation of the pressure gradient can be expressed as [24]:

$$|dp/dx| = (\mu/K) \cdot u + (F/\sqrt{K}) \cdot \rho u^2 \tag{47}$$

Figs. 5 and 6 indicate that the mass flow passes through the 635-mesh SS screen will have larger pressure losses than the other two do because the 635-mesh SS screen has the smallest porosity as shown in Table 2. For the same position in the regenerator, as the porosity decreases, $|u_1|$ will increases. It can be seen from Eq. (47) that if $|u_1|$ increases, the pressure gradient will increase accordingly.

Fig. 7 shows the variation of the amplitude of temperature T_{amp} in different radius equivalent circles at 60 K and 30 K, respectively. T_{amp} mean the amplitude of the mean temperature along the radial direction. The abscissa r denotes the radial distance between the

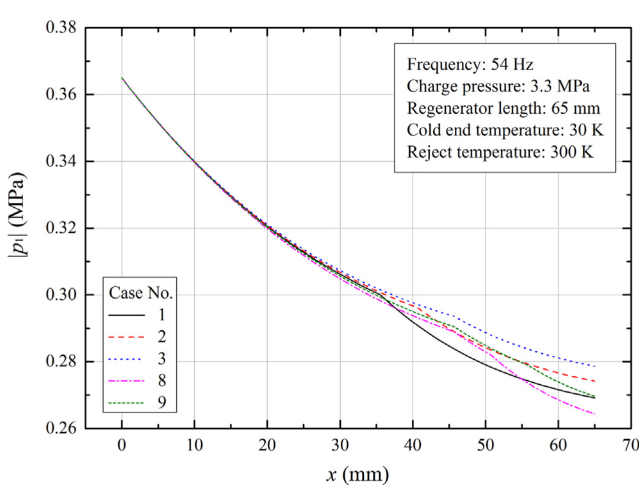

Fig. 5. Variations of the pressure amplitude of Case 1, Case 2, Case 3, Case 8 and Case 9 along the length, respectively.

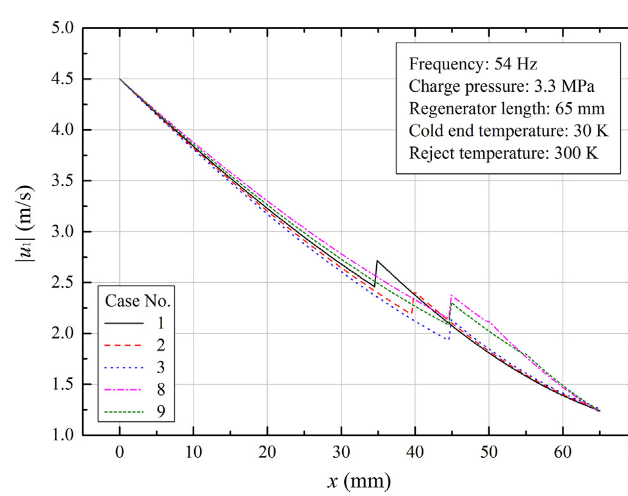

Fig. 6. Variations of the velocity amplitude of Case 1, Case 2, Case 3, Case 8 and Case 9 along the length, respectively.

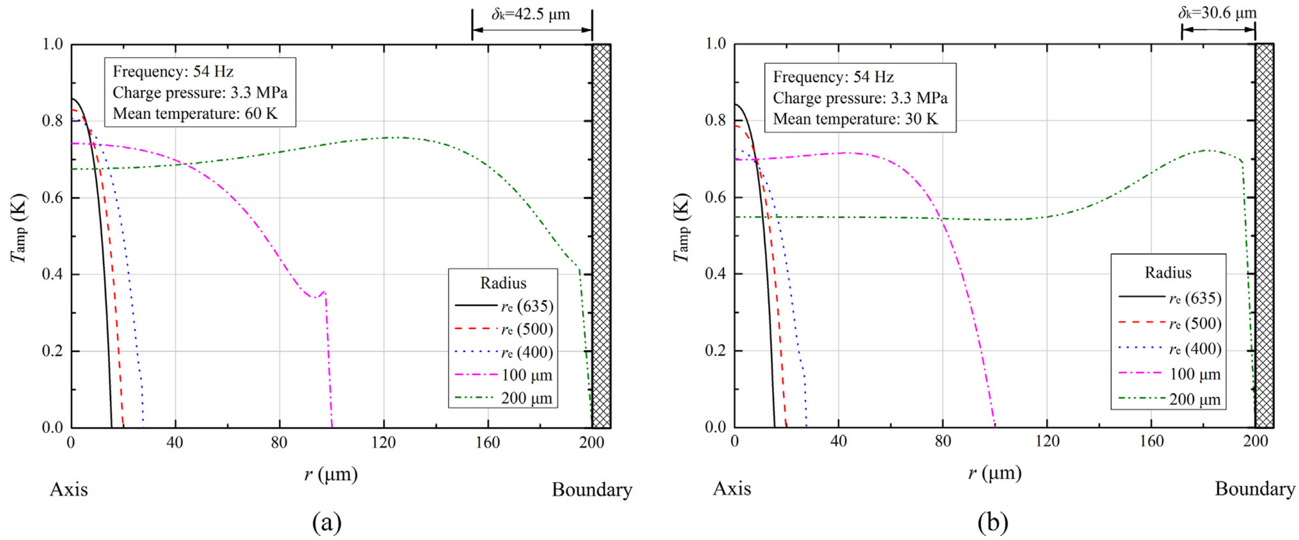

Fig. 7. Variation of the amplitude of temperature T_{amp} in different radius equivalent circles at 60 K and 30 K, respectively.

boundary and the axis. The thermal penetration depth at 60 K and 30 K is 42.5 μm and 30.6 μm, respectively. The two curves when r_e are 100 and 200 μm are given for comparisons. They indicate the distribution of T_{amp} when the radial distances r_e are far larger than the thermal penetration depth. The hydraulic diameters for 400-mesh, 500-mesh and 635-mesh SS screens are 55.24, 39.60 and 31.28 μm, respectively. And the equivalent radii of them are usually smaller than the thermal penetration depth below 60 K. In order to show the distribution of T_{amp} when the equivalent radii are far larger than the thermal penetration depth, the two curves for 100 and 200 μm are given. It is observed that when r_e equals 200 μm, which is about five to six times the thermal penetration depth, T_{amp} near the boundary is larger than that in axis. In the regenerator, the high frequency fluid has no enough time to take away the heat coming from the matrix immediately. As the radius decreases, T_{amp} at the axis becomes larger and the profile of T_{amp} is like the Poisson distribution. That means the fluid has the sufficient heat transfer for the small equivalent radius of the matrix.

Fig. 8 shows the profile of the amplitude of temperature T_{amp} with the constant matrix of 400-mesh or 635-mesh SS screens at different temperatures of 300 K, 180 K, 60 K and 30 K, respectively. It is observed that the profile of T_{amp} becomes smaller as the temperature decreases. The reason is that the thermal penetration depth decreases with the decrease of the temperature, which makes that the heat transfer at 30 K is worse than that at 300 K for the constant radius of the equivalent circle. The profile of the thermal characteristics decreases slightly from 300 K to 180 K but drops significantly from 180 K to 30 K. It indicates that the decrease of the thermal characteristics will become greater at lower temperature range. Therefore, the matrix with smaller porosity, such as 635-mesh SS screen, should be used at lower temperature to enhance the heat transfer.

Fig. 9 shows the one cycle of the dynamic pressure profile along the length for Case 8. It can be seen that the change of the phase angles between the inlet pressure and the outlet pressure is slight. The pressure amplitude decreases monotonically along the regenerator length. The turning points happen at the location of 45 mm and 51 mm from the regenerator inlet, both of which are the interfaces of the different screen meshes. Fig. 10 shows the one cycle of the dynamic velocity profile along the length for case 8. It can be seen that, compared to the pressure variations, the phase angles between the inlet velocity and the outlet velocity change

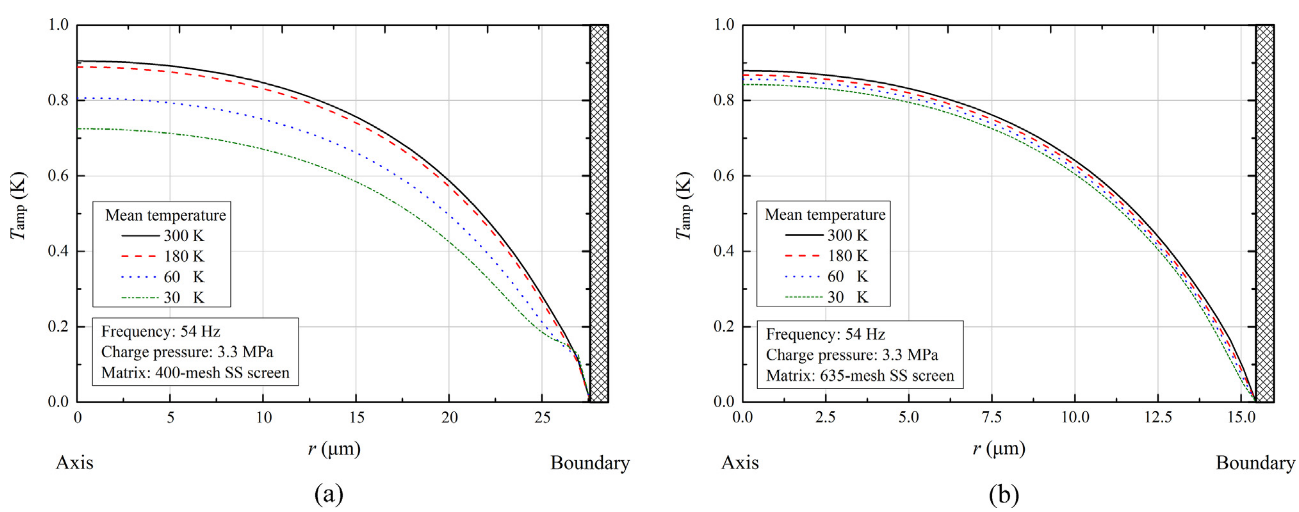

Fig. 8. Profile of the amplitude of temperature T_{amp} with the constant matrix of 400-mesh or 635-mesh SS screens at different temperatures of 300 K, 180 K, 60 K and 30 K, respectively.

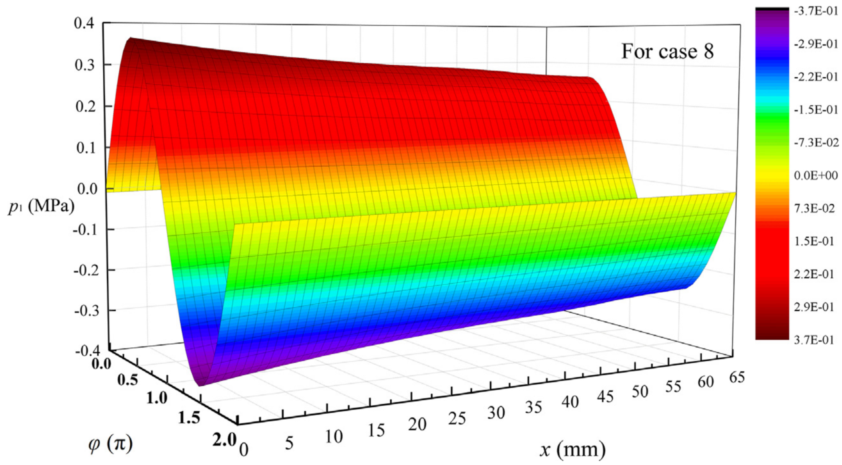

Fig. 9. One cycle of the dynamic pressure profile along the length for Case 8.

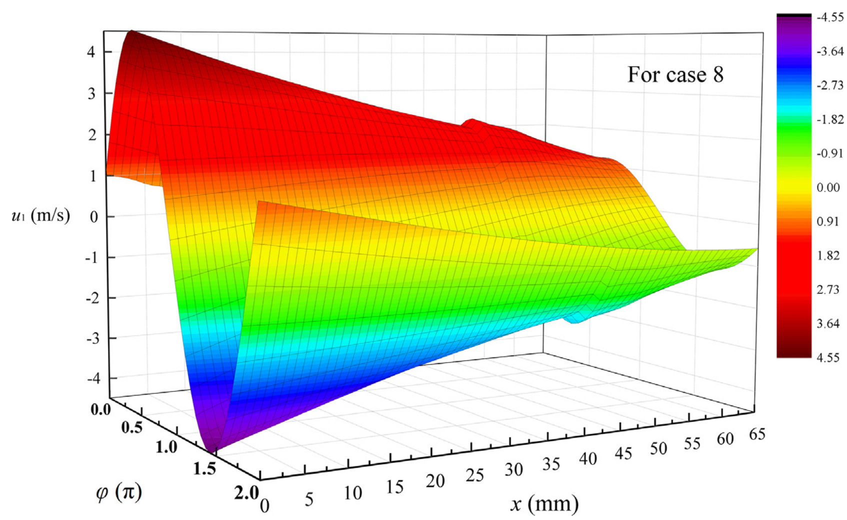

Fig. 10. One cycle of the dynamic velocity profile along the length for case 8.

significantly and the velocity amplitude reduces greatly. The change of the phase angle between the inlet and outlet velocity reaches 0.23π. Based on Figs. 9 and 10, the changes of p_1, u_1 and φ along the length can be observed directly. The phase difference of the pressure changes slightly while the one of the velocity varies significantly.

Fig. 11 shows the variations of the dynamic pressure and the velocity at inlet, midpoint and outlet of the regenerator for Case 8, respectively. It can be observed that the velocity leads the pressure at inlet, while the pressure leads the velocity at outlet. The phase shift between the velocity and the pressure are 0.078π at inlet and -0.152π at outlet. The pressure leads the velocity at inlet but lags behind at outlet. The amplitudes of both the pressure and the velocity at the outlet decrease because of the resistance of the matrix.

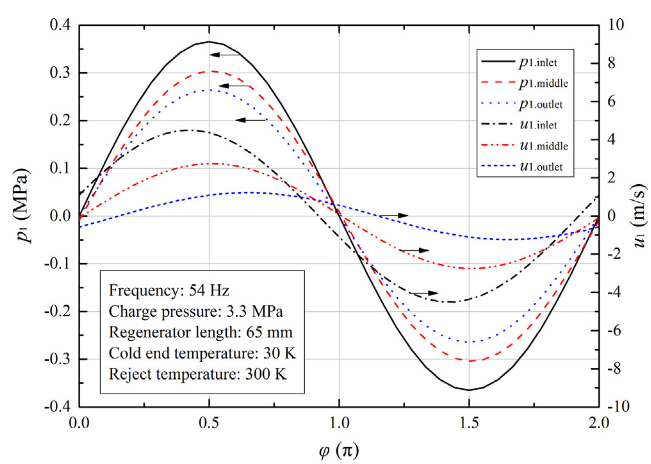

Fig. 11. Variations of the dynamic pressure and the velocity at inlet, midpoint and outlet of the regenerator for Case 8, respectively.

4.2. Experiment setup

Fig. 12 shows a schematic of a single-stage coaxial SPTC and its measurement system. The refrigeration system consists of the compressor, the pulse tube cold finger, and the connecting tube. The phase-shifter, excluding double-inlet and multi-bypass, uses the inertance tubes together with a gas reservoir to ensure the performance stability for the future practical applications. The dimensional parameters of the cold finger and the compressor are shown in Tables 1 and 3, respectively. The measurement system in the cold finger consists of four devices for measuring the pressure at out of the compressor, the displacement of the piston

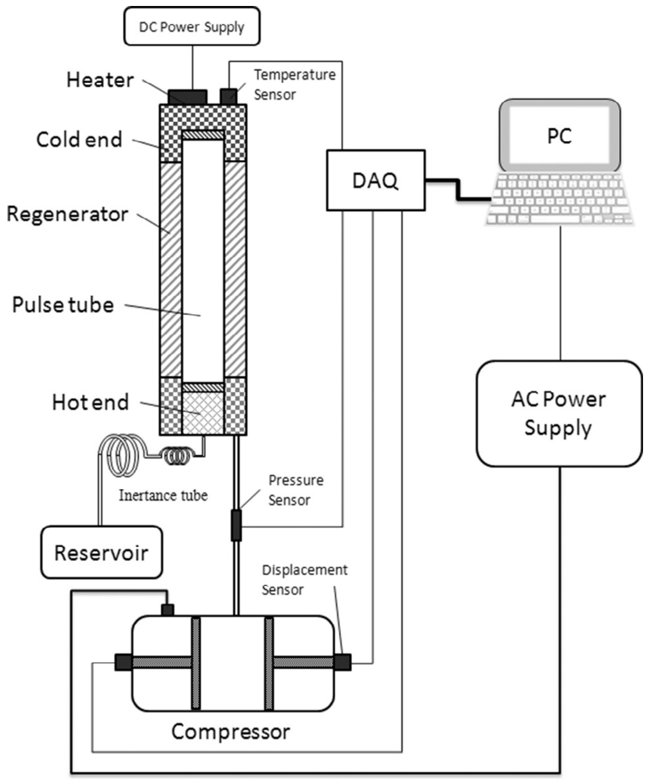

Fig. 12. Schematic of a single-stage coaxial SPTC and its measurement system.

Table 3
Parameters of the linear compressor.

Parameters	Values
Piston diameter	20 mm
Maximum displacement of single piston	6.5 mm
Cylinder volume	8.5 cm^3

in the compressor, the cooling capacity and the cold end temperature. Two linear variable differential transformers position transducers are fixed on the end of the pistons to measure the displacements. A piezoelectric pressure sensor is set at the outlet of the compressor to monitor the pressure. Temperature sensors and heaters are attached on the cold end to monitor the temperature and to provide the heat load, respectively. A multi-channel DAQ is developed to collects the data of all kinds of the sensors and sends to the computer.

Fig. 13 shows the actual experimental setup, in which the AC power supply is used to adjust the input electric power. The pressure sensor is set at the inlet of the cold finger to monitor both the dynamic pressure and its phase angles relative to the mass flux is measured by the displacement sensors. The cold tip temperature is monitored by the temperature sensors attached on the cold heat exchanger, and the heat load is provided by the heaters with the DC power supply. The tested data are collected by the DAQ and transferred to the PC.

4.3. Experimental verifications

The performance characteristics of the SPTC with constant SS mesh matrix are investigated firstly. The measured values are the temperature T_h, the amplitude of the velocity $|u_1|$, the amplitude of the pressure $|p_1|$ and the phase angle φ between $|p_1|$ and $|u_1|$ at the inlet of the regenerator, and temperature T_c at the cold tip, which are the boundary conditions as same as those used in the simulations.

Table 4 shows the experimental average pressure amplitude, velocity and their phase angle with the same PV works at inlet as that used in the simulation. It is observed that when the frequency increases from 50 Hz to 58 Hz, $|p_1|$ decreases while $|u_1|$ and φ increase. The phase angle changes significantly from 0.031π to 0.128π.

Fig. 14 shows the variations of the experimental and simulated cooling capacity with the frequency, respectively. It is observed that the best performance occurs at 54 Hz with the 400-mesh SS

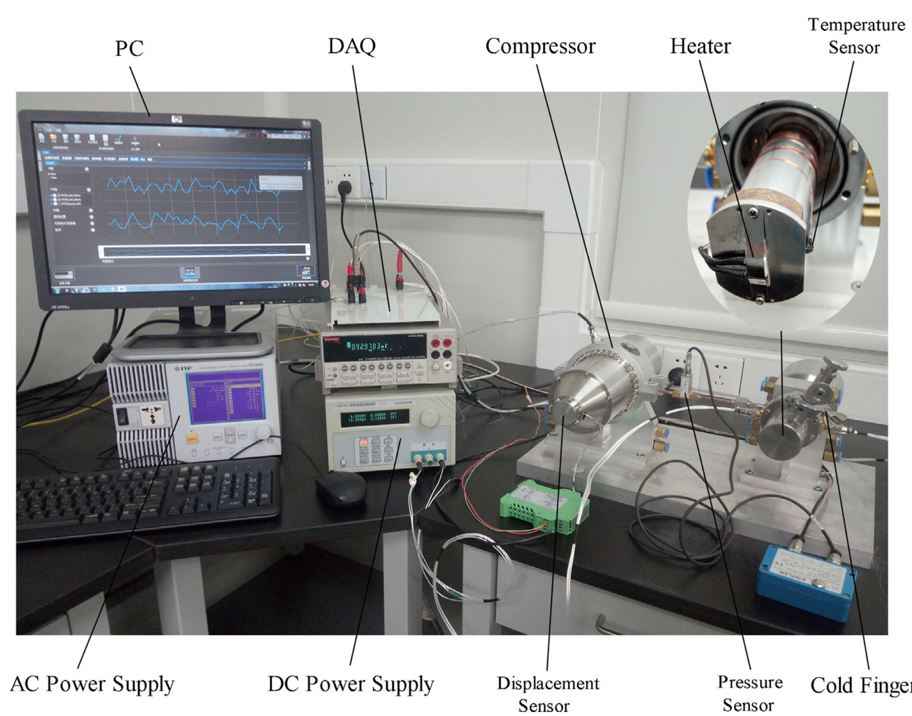

Fig. 13. Experimental setup.

Table 4
Boundary conditions and PV work of the regenerator.

Frequency (Hz)	$\|p_1\|$ (MPa)	$\|u_1\|$ (m/s)	$\varphi(\pi)$	PV work (W)
50	0.3688	4.41	0.031	165.64
52	0.3675	4.46	0.055	165.24
54	0.3650	4.51	0.078	163.39
56	0.3640	4.65	0.094	165.73
58	0.3600	4.83	0.128	163.68

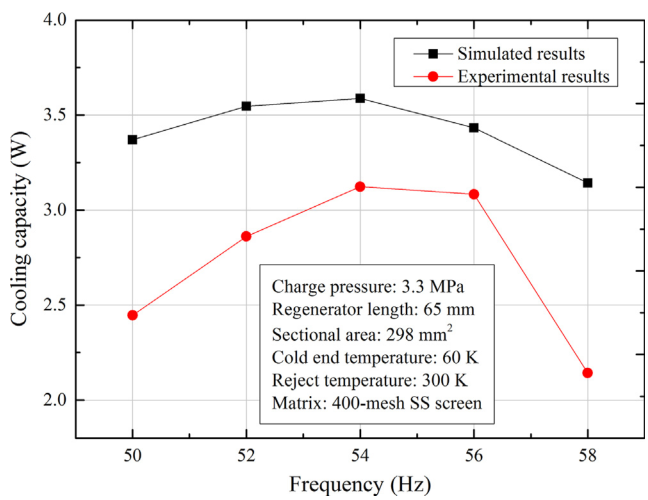

Fig. 14. Variations of the experimental and simulated cooling capacity with the frequency, respectively.

screen, which can provide 3.12 W at 60 K with an input PV power of 163.39 W, compared to the best simulated performance of 3.58 W at 60 K at 54 Hz with the same PV power. Fig. 14 shows the variations of the cooling capacity with the operating frequency. It should be mentioned that the model is mainly based on the assumption that the SPTC operates near the optimal frequency. For example, in the frequency range of 54 Hz to 56 Hz, the numerical and experimental have the similar changing tendencies, and the largest difference between them is about 12.5%, which indicates that the developed model is quite reasonable. However, when the actual operating frequencies significantly deviate from the optimal frequency, such as at 50 Hz and 58 Hz, the SPTC will work under terrible conditions and thus many unexpected actual losses occur, the differences between the simulated and actual results will become larger and larger, such as even up to 40%, and then these values are used only for reference.

Fig. 15(a) shows the variations of the simulated and experimental cooling capacities with the cold end temperature for Case 8 and Case 13, respectively. For both cases, the operating frequency and the charge pressure are 54 Hz and 3.3 MPa, respectively. The input electric power is set at 240 W with the motor efficiency of 70.3%, thereby providing the same input condition with the simulations, in which the PV work of about 165 W from the compressor is used. It is observed that there are good agreements about the changing tendencies between simulated and experimental results for both Case 8 and Case 13. And the simulated and experimental cooling capacities in Case 8 are obviously higher than those in Case 13.

Fig. 15(b) shows the comparisons between the typical one-dimensional simulation result and the one gotten by the developed two-dimensional model in this paper for Case 8. The one-dimensional result has been acquired by Regen 3.3, which is the popular one-dimensional simulation software for the regenerator. As shown in Fig. 15(b), the two-dimensional simulation result is much closer to the experimental one, and the one-dimensional result is obviously higher than the two-dimensional one, which means that the widely-used one dimensional model neglects several irreversible losses. As shown in Eqs. (21)–(24), the radial direction dependence of the temperature and the velocity vibration are considered in the developed two-dimensional model but neglected by the one-dimensional software.

Fig. 16(a) shows the variations of the simulated and experimental cooling capacities with the cold end temperature for Case 8 and Case 12, respectively. For both cases, the operating frequency and the charging pressure are 52 Hz and 3.4 MPa, respectively. The reject temperature is 300 K and the input electric power is set at 220 W, which is equal to the input PV power of about 170 W in the simulations. It is observed that there are good agreements about the changing tendencies between simulated and experimental results for Case 8 and Case 12. In the experiments, a cooling power of 0.45 W at 30 K for Case 8 has been achieved, which is about 0.16 W higher than the experimental result for Case 12 achieved previously[10]. And the no-load temperature has been further decreased from 27. 2 K to 26.7 K.

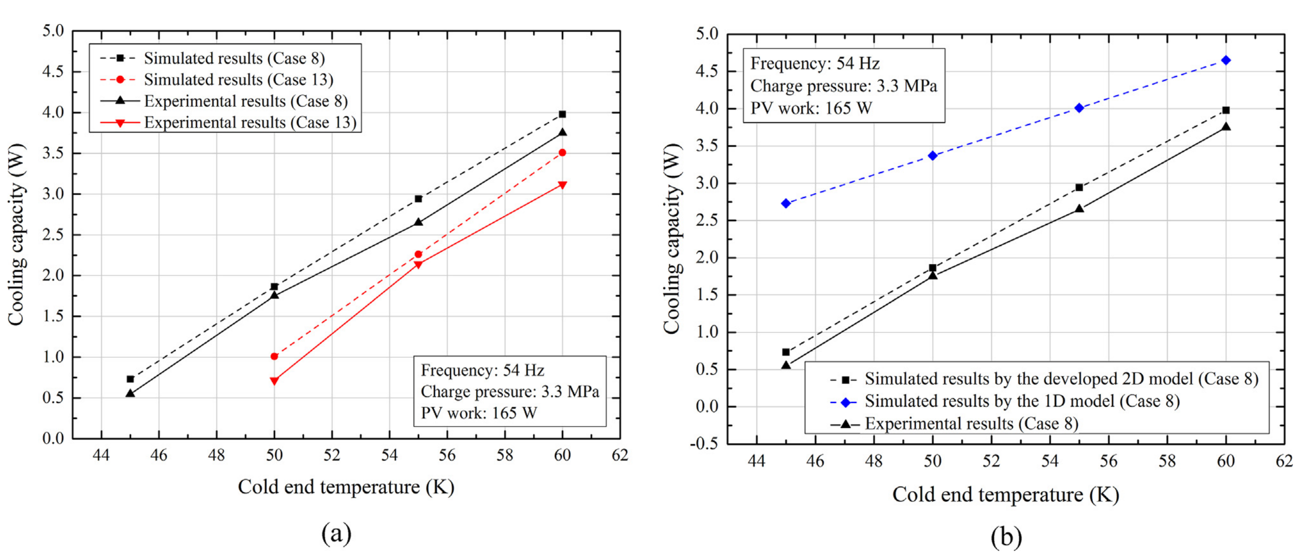

Fig. 15. (a) Variations of simulated and experimental cooling capacities with cold end temperature for Case 8 and Case 13, respectively; (b) Comparisons between the typical one-dimensional simulation result and the one gotten by the developed two-dimensional model for Case 8.

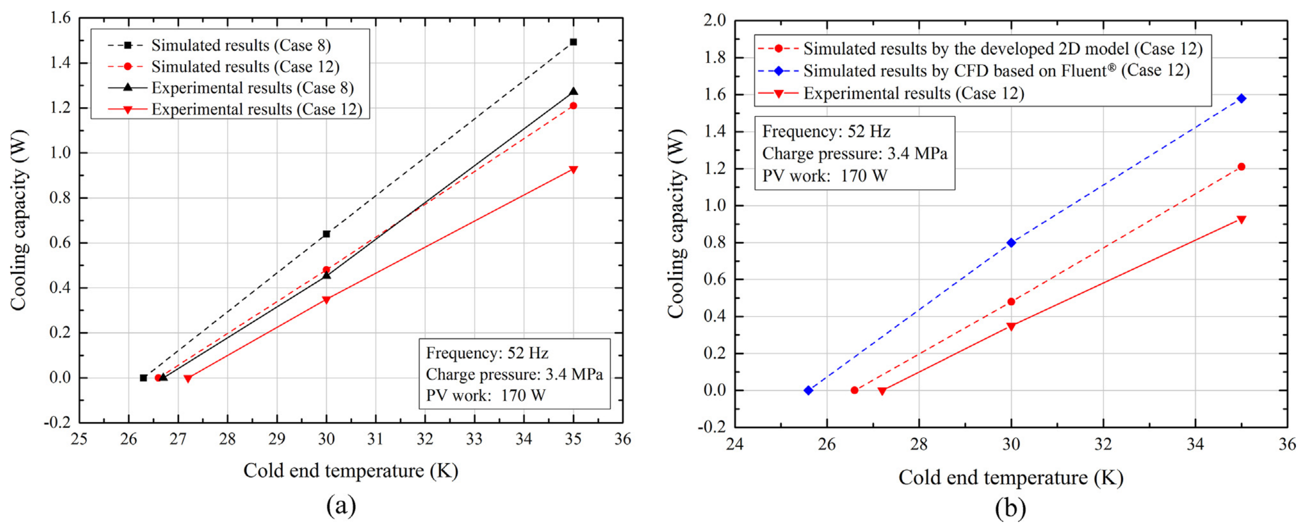

Fig. 16. (a) Variations of simulated and experimental cooling capacities with cold end temperature for Case 8 and Case 12, respectively; (b) Comparisons between the CFD result in Ref. [10] and the one gotten by the developed two-dimensional model for Case 12.

Fig. 16(b) shows the comparisons between the CFD simulation result based on the Fluent® approach in Ref. [10] and the one gotten by the developed two-dimensional model in this paper for Case 12. It should be noted that the CFD simulation in Ref. [10] was made in the same laboratory and it was based on the same conditions as those for the developed two-dimensional model in this paper for Case 12. And thus the comparisons are meaningful. It can found that the changing tendencies of the two simulation curves are very similar, and both results are close to the experimental result. Thereby, the experiments verify the rationality of the two-dimensional model built in this paper. And furthermore, compared to the CFD model based on Fluent®, the developed two-dimensional model in this paper is time-saving and does not take up much computing resources.

5. Conclusions

The regenerator is one of the key components for the regenerative cryocooler because the irreversible loss caused in it usually accounts for an overwhelming proportion of the overall ones.

In this paper, the developed two-dimensional model has been compared with both the one-dimensional model and the CFD model based on the Fluent® approach. On the one hand, the experimental results indicate that the developed two-dimensional model is much more accurate than the one-dimensional one. On the other hand, the results based on the developed model are close to the CFD simulation based on Fluent®, and also can be verified by the experiments, and furthermore, this calculating process is much faster than the latter.

Based on the developed model, the regenerator with mixed matrices for optimizing the SPTC is established, in which the different filling proportions of mixed matrices made of stainless steel screens are studied and compared, and then the optimal filling proportion with the combination of 400-mesh, 500-mesh and 635-mesh SS screens is suggested.

The experiments are then conducted to verify the validity of the theoretical investigations based on a single-stage coaxial SPTC, in which the cooling characteristics with various frequencies and temperatures are tested and then compared with the analyses. The results show a good agreement between simulations and experiments when the operating frequencies are close to the optimal one. The cooling performance can be enhanced by the optimized mixed matrix acquired by the developed model.

For a reject temperature of 300 K and an input electric power of 220 W, the single-stage coaxial SPTC has experimentally achieved the cooling capacity of 0.45 W at 30 K and a no-load temperature of 26.7 K. The performance is impressive considering that only the conventional stainless steel matrices are employed and neither double-inlet nor multi-bypass phase-shifting approach is used.

Acknowledgements

The work is financially supported by The National Basic Research Program of China (2013CB632802), The Aeronautical Science Foundation of China (20162490005) and The Science and Technology Commission of Shanghai Municipality (15521104900).

Appendix A

In this appendix, we present the derivation process of Equation set (37).

Substituting Eqs. (16) and (17) into Eq. (33) and performing the integration yields the first equation in Equation set (37) as follow:

$$E_2 = X_1 - X_3 + \nabla T_m \cdot (X_2 - \pi R^2 k) \tag{A.1}$$

where X_1, X_2 and X_3 are expressed as:

$$X_1 = \frac{\pi R^2 \phi \beta T_m}{2\omega \rho_m \sigma} \cdot \mathrm{Im}[f_{X1}(\phi \nabla \tilde{p}_1 + \omega \rho_m A_0) p_1 / \tilde{\alpha}^2] \tag{A.2}$$

$$X_2 = -\frac{\pi R^2 \phi c_p}{2\omega^3 \rho_m \sigma} \cdot \mathrm{Im}[f_{X2}(\phi \nabla \tilde{p}_1 + \omega \rho_m A_0)(\phi \nabla p_1 + \omega \rho_m A_0)/(\alpha^2 \tilde{\alpha}^2)] \tag{A.3}$$

$$X_3 = \frac{\pi R^2 \phi}{2\omega \rho_m}(1 - T_m \beta) \cdot \mathrm{Im}[(1 - f_v)(\phi \nabla p_1 + \omega \rho_m A_0)\tilde{p}_1 / \alpha^2] \tag{A.4}$$

f_{X1}, f_{X2} and A_0 in X_1 and X_2 are expressed as:

$$f_{X1} = 1 - \tilde{f}_v + \frac{\alpha^2(\tilde{f}_v - f_k)}{Pr\sigma + \alpha^2} \tag{A.5}$$

$$f_{X2} = 1 - \tilde{f}_v + \frac{1}{2}\frac{Pr\sigma(\tilde{f}_v - f_v)}{Pr\sigma - \alpha^2} + \frac{\alpha^4(f_k - \tilde{f}_v)}{(Pr\sigma - \alpha^2)(Pr\sigma + \alpha^2)} \tag{A.6}$$

$$A_0 = \frac{F\phi}{\omega\sqrt{K}} u_0^2 \tag{A.7}$$

Substituting Eqs. (14), (18) and (19) into Eq. (11) yields the second equation in equation set (37) as follow:

$$\nabla^2 p_1 = Y_1 \cdot p_1 - Y_2 \cdot p_1/T_m + Y_3 \cdot \nabla T_m \nabla p_1/T_m + Y_4 \cdot \nabla T_m/T_m \tag{A.8}$$

where Y_1, Y_2, Y_3 and Y_4 are expressed as:

$$Y_1 = \frac{\alpha^2\omega^2\phi\beta}{c_p\sigma}\left(\frac{1-f_k}{1-f_v}\right) \tag{A.9}$$

$$Y_2 = \frac{\alpha^2\omega^2}{ZR_g(1-f_v)} \tag{A.10}$$

$$Y_3 = \frac{1}{1-f_v}\left\{(b+1)[f_1 - (\alpha^2-2)(1-f_v)]/\alpha^2 - \left(1 - \frac{Pr\sigma f_v}{Pr\sigma-\alpha^2} + \frac{\alpha^2 f_k}{Pr\sigma-\alpha^2}\right)\Big/\sigma\right\} \tag{A.11}$$

$$Y_4 = \frac{A_0\omega\rho_m}{1-f_v}\left\{\{\alpha^2(1-f_v) - (b+1)[f_1 - (\alpha^2-2)(1-f_v)]\}/\alpha^2 - \left(1 - \frac{Pr\sigma f_v}{Pr\sigma-\alpha^2} + \frac{\alpha^2 f_k}{Pr\sigma-\alpha^2}\right)\Big/\sigma\right\} \tag{A.12}$$

The tilde denotes complex conjugate, and ∇p_1 and ∇T_m represent the pressure gradient and the mean temperature gradient along x-direction, respectively.

References

[1] G. Walker, Cryocoolers, First ed., Plenum Press, New York, 1983.
[2] I. Rühlich, H. Quack, Investigations on regenerative heat exchangers, Cryocoolers 10 (2002) 265–274.
[3] G.W. Swift, W.C. Ward, Simple harmonic analysis of regenerators, J. Thermophys. Heat Transfer 10 (1996) 652–662.
[4] Y.L. Ju, C. Wang, Y. Zhou, Numerical simulation and experimental verification of the oscillating flow in pulse tube refrigerator, Cryogenics 38 (1998) 169–176.
[5] X.H. Hao, Y.L. Ju, Experimental study on the low temperature regenerator packed with rectification meshes, Cryogenics 50 (2010) 390–396.
[6] Y.L. He, C.F. Zhao, W.J. Ding, W.W. Yang, Two-dimensional numerical simulation and performance analysis of tapered pulse tube refrigerator, Appl. Therm. Eng. 27 (2007) 1876–1882.
[7] Y.L. He, Y.B. Tao, F. Gao, A new computational model for entire pulse tube refrigerators: Model description and numerical validation, Cryogenics 49 (2009) 84–93.
[8] M.Y. Xu, T. Morie, Numerical simulation of 4K GM cryocooler, Cryocoolers 17 (2002) 253–259.
[9] H.Z. Dang, L. Zhang, J. Tan, Dynamic and thermodynamic characteristics of the moving-coil linear compressor for the pulse tube cryocooler: Part A: Theoretical analyses and modeling, Int. J. Refrig. 69 (2016) 497–504.
[10] H.Z. Dang, Y.B. Zhao, CFD Modelling and experimental verification of a single-stage coaxial Stirling-type pulse tube cryocooler without either double-inlet or multi-bypass operating at 30–35 K using mixed stainless steel mesh regenerator matrices, Cryogenics 78 (2016) 40–50.
[11] Fluent 6.3 User's Guide, Fluent Inc. <http://www.fluentusers.com>.
[12] D.A. Nield, A. Bejan, Convection in porous media, Third ed., Springer Science & Business Media, New Zealand, 2006.
[13] M. Lewis, R. Radebaugh, Measurement of heat conduction through metal spheres, Cryocoolers 11 (2001) 419–425.
[14] S.H. Tasnim, S. Mahmud, R.A. Frase, I. Pop, Brinkman-Forchheimer modeling for porous media thermoacoustic system, Int. J. Heat Mass Transfer 54 (2011) 3811–3821.
[15] G.W. Swift, S.L. Garrett, Thermoacoustics: A unifying perspective for some engines and refrigerators, Fifth ed., Los Alamos, 2001.
[16] S. Choi, K. Nam, S. Jeong, Investigation on the pressure drop characteristics of cryocooler regenerators under oscillating flow and pulsating pressure conditions, Cryogenics 44 (2004) 203–210.
[17] National Institute of Standards and Technology, REGEN PACKAGES. <http://math.nist.gov/~AOGallagher/auxfiles/regenstart.html>, 2009.
[18] J. Olson, G.W. Swift, Suppression of acoustic streaming in tapered pulse tubes, Cryocoolers 10 (2002) 307–313.
[19] J.C. Butcher, Implicit Runge-Kutta Processes, Math. Comput. 18 (1964) 50–64.
[20] J.C. Butcher, Runge-Kutta methods in modern computation part I: Fundamental Concepts, Comput. Phys. 8 (1994) 411–415.
[21] H.Z. Dang, Development of high performance moving-coil linear compressors for space Stirling-type pulse tube cryocoolers, Cryogenics 68 (2015) 1–18.
[22] H.Z. Dang, 40 K single-stage coaxial pulse tube cryocoolers, Cryogenics 52 (2012) 216–220.
[23] Z.Q. Gao, H.Z. Dang, Entropy analyses of the three-stage thermally-coupled Stirling-type pulse tube cryocooler, Appl. Therm. Eng. 100 (2016) 944–960.
[24] R.C. Tew, T. Simon, D. Gedeon, et al., An initial non-equilibrium porous-media model for CFD simulation of Stirling regenerators. in: Proceedings of the 4th International Energy Conversion Engineering Conference, 2006.